PHYSICAL REVIEW C **96**, 044621 (2017)

Cross section measurement for the ^{10}B($n,t2\alpha$) three-body reaction at 4.0, 4.5, and 5.0 MeV. II. Experimental setup and results

Zhimin Wang,[1,2] Huaiyong Bai,[1] Luyu Zhang,[1] Haoyu Jiang,[1] Yi Lu,[1] Jinxiang Chen,[1] Guohui Zhang,[1,*] Yu. M. Gledenov,[3]
M. V. Sedysheva,[3] and G. Khuukhenkhuu[4]

[1] *State Key Laboratory of Nuclear Physics and Technology, Institute of Heavy Ion Physics, Peking University, Beijing 100871, China*
[2] *Department of Physics, School of Information Science and Engineering, Ocean University of China, Qingdao 266100, China*
[3] *Frank Laboratory of Neutron Physics, Joint Institute for Nuclear Research, Dubna 141980, Russia*
[4] *Nuclear Research Centre, National University of Mongolia, Ulaanbaatar 17032, Mongolia*

(Received 29 June 2017; published 24 October 2017)

Cross sections of the ^{10}B($n,t2\alpha$) three-body reaction were measured at $E_n = 4.0$, 4.5, and 5.0 MeV using a twin gridded ionization chamber and a thin-film ^{10}B sample. The present paper is the second part of the work. A digital data-acquisition system was developed for the gridded ionization chamber based on the waveform digitizer. A thin-film ^{10}B sample was designed and prepared. The number of ^{10}B atoms in the sample was determined by the relative method using the thermal neutron induced ^{10}B(n_{th},α)^{7}Li and ^{6}Li(n_{th},t)^{4}He reactions with a ^{6}LiF sample as the reference. The measurement of the ^{10}B($n,t2\alpha$) reaction was performed at the 4.5 MV Van de Graaff accelerator of Peking University. In the measurement, the double-coincidence technique was used, which involves the forward-backward and the grid-anode coincidence. In the data processing, the effective event area in the forward two-dimensional spectrum and the time window in the drift-time spectrum were employed to reject the background events. Cross sections of the ^{10}B($n,t2\alpha$) and ^{10}B(n,α)^{7}Li reactions were obtained. The present results are compared with the data of existing measurements and evaluations.

DOI: 10.1103/PhysRevC.96.044621

I. INTRODUCTION

The ^{10}B($n,t2\alpha$) three-body reaction was measured by the forward-backward coincidence method using a thin-film ^{10}B sample and a twin gridded ionization chamber (GIC). The present paper is the second part of the work. In the first paper [1], we introduced how to calculate the complete final-state phase space of the ^{10}B($n,t2\alpha$) reaction and to predict the experimental spectrum measured by the GIC detector. To be able to implement the measurement of the ^{10}B($n,t2\alpha$) reaction, in addition to the prediction of the spectrum, there are two other works that need to be done: (1) development of the GIC spectrometer based on a waveform digitizer (WFD) and (2) preparation of a thin-film ^{10}B sample and determination of the number of ^{10}B atoms in the sample. In the present paper, the WFD-based GIC spectrometer and the thin-film ^{10}B sample are shown in Secs. II and III, respectively. Section IV shows the measurement of the ^{10}B($n,t2\alpha$) reaction including the experimental details, the data processing, and the measured results. The conclusions are given in Sec. V.

II. THE WFD-BASED GIC SPECTROMETER

The charged particle spectrometer consists of a twin GIC and a digital data-acquisition (DAQ) system as shown in Fig. 1. The geometry of the double section of the ionization chamber is symmetric with a common cathode. Distances from the cathode to the grid, from the grid to the anode, and from the anode to the shield are 61, 15, and 9 mm, respectively. A sample changer is set at the common cathode with five sample positions. The geometric structure of the sample position is well shaped and the sample is mounted on the bottom of the well. Double samples with thick backing can be placed back to back at one of the positions. In the present work, one ^{10}B sample with thin backing and one background sample were placed at the first and second sample positions, respectively. A ^{6}LiF sample with thick backing was placed at the backward direction of the third position of the sample changer. These three samples are described in the next section. In addition, a ^{238}U film sample (493.6 μg/cm^2, ^{238}U only) was placed at the backward direction of the fourth position; double compound α sources with thick backing were placed back to back at the fifth position. Details of the GIC detector can be found in Ref. [2].

To perform the full-waveform recording of the signals from the GIC detector, we developed a new digital DAQ system based on the high-speed WFD. The digitizer (PDA14, Signatec, 14 bit) has two input channels. The maximum digitization rate is 100 MHz, namely, 10 ns, for each data sample. Two digitizers were employed to record the two grid and two anode signals of the GIC as shown in Fig. 1. Since forward and backward emitted particles from the ^{10}B($n,t2\alpha$) reaction would induce signals simultaneously on the common cathode, the cathode signal was not recorded. The PDA14 boards are plugged into a computer directly and data are transferred from the digitizer to the PC through the PCI-X buses.

The two PDA14 boards can be operated in two configurations: the single board operation and the master-slave operation. In the single board operation, the two boards work independently. In the master-slave operation, the master board drives the clock and triggers signals for the slave board, and the data on the slave boards align sample for sample with the data on the master board. By the master-slave configuration,

---

[*] Corresponding author: guohuizhang@pku.edu.cn

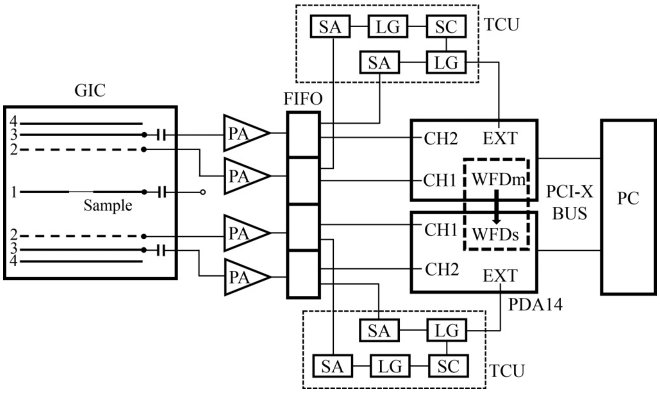

FIG. 1. Block diagrams of the electronics of the GIC spectrometer: 1, cathode; 2, grid; 3, anode; 4, shield; PA, preamplifier; FIFO, quad fan in, fan out; SA, spectroscopy amplifier; LG, linear gate stretcher; SC, single-channel analyzer; CH, input channel; EXT, external trigger; WFDm, WFD master; and WFDs, WFD slave.

the forward and backward signals of the GIC can be recorded coincidently.

A versatile data-acquisition software was developed using the LABVIEW language to control the PDA14 digitizers and perform online data processing. The classical producer-consumer pattern was adopted in the structure of the program to improve the efficiency of the software. The "producer" manages the data transmission from the digitizers to the memory of the PC. The "consumer" does the online data processing and then displays the measured results in real time and saves the waveform data onto the hard disk of the PC.

In order to improve the antinoise performance of the GIC spectrometer, the PDA14 boards were configured to use the external trigger. A trigger control unit (TCU) was built up for each of the two PDA14 boards to produce external trigger signals using the nuclear instrument modules (NIM). The trigger signals are produced through the coincidence between the grid and the anode signals of the GIC detector. As shown in Fig. 1, both the grid and the anode preamplifier signals are first split into two without amplitude attenuation using the quad fan in/fan out (FIFO) module (N625, CAEN), and then one is fed into the digitizer and the other is fed into the TCU. In the TCU, the grid and the anode signals are first processed by the spectroscopy amplifier (ORTEC, 572A) and the linear gate stretcher (ORTEC, 542). The 542 module of the grid operates in the NORMAL mode and the anode's 542 module operates in the GATED/COINC mode. The output of the grid's 542 module is fed into the single-channel analyzer, and then the single-channel analyzer's output is fed into the gate input of the anode's 542 module. In fact, the coincidence between the grid and the anode signals is completed in the anode's 542 module. The output of the anode's 542 module is fed into the digitizer as the trigger signal. Since the amplitude of the output of the 542 module is proportional to that of the amplifier pulse, the amplitude of the trigger signal is proportional to that of the anode's amplifier pulse.

The WFD-based spectrometer has three advantages: (1) the waveforms of the preamplifier signals from the GIC detector are recorded, which allows one to optimize the settings for best signal treatment during offline analysis using digital signal processing (DSP) technology [3]; (2) independent and coincident measurement of the forward and backward signals of the GIC detector can be achieved easily by changing the operational configurations of the two PDA14 boards; and (3) the antinoise performance is good because the external trigger signals are produced through the coincidence of the grid and the anode signals, and the signal-to-noise ratio of the grid and anode signals is high after being processed by the spectroscopy amplifier and the linear gate stretcher.

III. THE THIN-FILM ^{10}B SAMPLE

To measure the three particles emitting forward and backward from the $^{10}\mathrm{B}(n,t2\alpha)$ reaction simultaneously, the solid ^{10}B sample should be thin enough. However, the thin sample should be stable and robust against being broken during the transportation, installation, and experiment. In the present work, a thin-film ^{10}B sample fulfilling the above requirements was designed and prepared. The thin-film ^{10}B sample consists of four components: the ^{10}B deposit, the aluminum-film backing, the tantalum frame, and the aluminum washer.

When a self-supporting ^{10}B sample is very thin, it becomes extremely easy to break. Therefore, the ^{10}B material was deposited through vacuum evaporation onto the aluminum-film backing. The thickness of the aluminum backing is about 0.16 μm.

The tantalum (Ta) frame was used as the supporter of the aluminum backing. The diameter of the Ta frame is 48.0 mm and the thickness is 0.1 mm. There are 1 circular and 24 fan-shaped holes arranged regularly in the Ta frame as shown in Fig. 2. The diameter of the innermost circular hole is 5.0 mm. The intermediate eight fan-shaped holes feature 5.5- and 11.5-mm inner and outer radii, respectively, with a central angle of 30° and the outermost 16 fan-shaped holes feature 14.0- and 20.0-mm inner and outer radii, respectively, with a central angle of 15°. The holes were machined using the laser cutting technique.

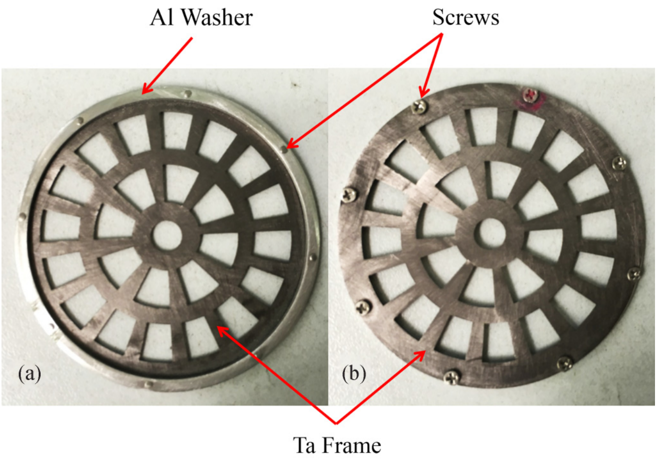

FIG. 2. The tantalum supporter with the aluminum washer viewed from side A and side B.

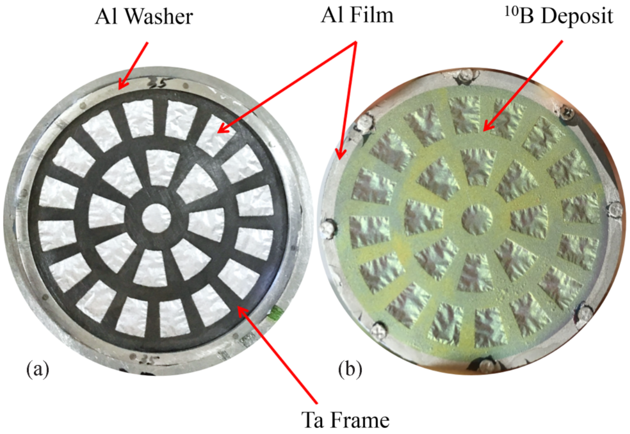

FIG. 3. The thin-film ^{10}B sample viewed from side A and side B.

After the process of laser cutting, the Ta frame deformed to some degree. An aluminum washer was used to stretch and flatten the Ta frame. The Ta frame was fixed on the washer through eight screws as shown in Fig. 2.

The thin-film ^{10}B sample was prepared at the China Institute of Atomic Energy (CIAE). In the process of preparation, the aluminum backing was made first through vacuum evaporation by the resistance heating method. The aluminum material was evaporated onto a glass sheet covered with the release agent. Since the release agent is water soluble, when the glass sheet was in the water, the aluminum film was released from the glass sheet and floated in the water. Then the Ta frame was used to salvage the aluminum film and they stuck together by themselves. The thickness of the aluminum film was determined by the weighing method. The inhomogeneity of the thickness was about 5%, which was calibrated by cutting the monitor film into several circular areas with same diameter and weighing them.

The aluminum film was on side B of the Ta frame and the ^{10}B material was evaporated onto the aluminum backing by the electron beam bombardment method [4]. The evaporation process was carefully controlled to guarantee that no ^{10}B material was deposited on the opposite side of the aluminum backing (i.e., side A of the Ta frame). Figure 3 displays the thin-film ^{10}B sample. The diameter of the ^{10}B deposit is 43.3 mm. The enrichment of the ^{10}B is 94%.

In addition to the ^{10}B sample, a thin-film background sample was also prepared without the ^{10}B deposits on the aluminum backing. The thickness of the aluminum backing is the same as that for the ^{10}B sample. The background sample is used for the background measurement in the measurement of the ^{10}B$(n,t2\alpha)$ reaction.

In preparing the reference ^{6}LiF sample, the lithium fluoride was evaporated onto a tantalum-foil backing (Φ48.0 mm × 0.1 mm) without holes. The enrichment of the ^{6}Li is 90%. The diameter of the ^{6}LiF deposit is the same as that of the ^{10}B deposit (43.3 mm). The thickness of the ^{6}LiF deposit is 94.5 μg/cm^2. The number of ^{6}Li atoms is 3.03×10^{19} with an uncertainty of 3%.

Before using the thin-film ^{10}B sample to measure the ^{10}B$(n,t2\alpha)$ three-body reaction, the number of ^{10}B atoms in the sample, especially the number of ^{10}B atoms in the position of holes, needed to be determined. The relative comparison method was used by measuring the thermal neutron induced ^{10}B$(n_{th},\alpha)^7$Li and ^{6}Li$(n_{th},t)^4$He reactions with the ^{6}LiF sample as the reference [5]. When the neutron fluence passing through the ^{10}B and ^{6}LiF samples is equal, the number of ^{10}B atoms, N_B, can be calculated by the following equation:

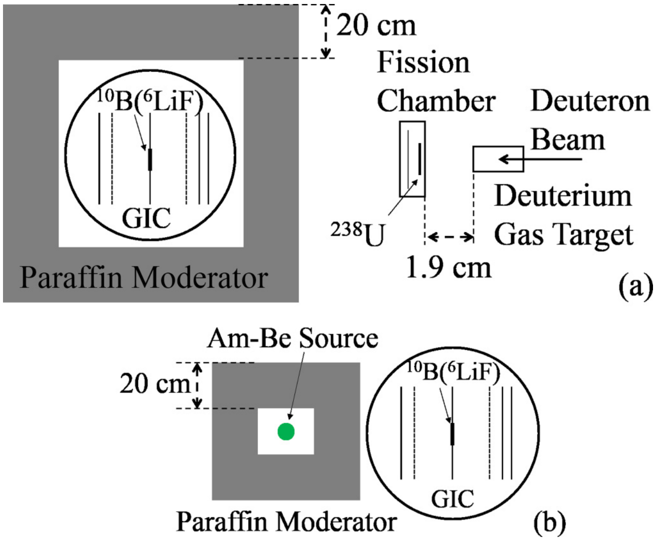

FIG. 4. Schematics of the experimental setup viewed from top, based on (a) the accelerator d-d neutron source and (b) the Am-Be neutron source.

$$N_{\mathrm{B}} = N_{\mathrm{Li}} \frac{N_\alpha}{N_t} \frac{\sigma_t}{\sigma_\alpha}, \tag{1}$$

where N_{Li} is the number of ^{6}Li atoms; N_α and N_t are the event counts of the ^{10}B$(n_{th},\alpha)^7$Li and ^{6}Li$(n_{th},t)^4$He reactions, respectively; and σ_α and σ_t are the cross sections of the ^{10}B$(n_{th},\alpha)^7$Li and ^{6}Li$(n_{th},t)^4$He reactions, respectively, which are the standard cross sections [6]. At $E_n = 0.0253$ eV, σ_t is equal to 938 b and $\sigma_\alpha = 3843$ b, so the ratio of σ_t to σ_α is equal to 0.2441. In fact, this ratio remains a constant for neutrons with energy below 0.01 MeV because cross sections of both the ^{10}B$(n_{th},\alpha)^7$Li and ^{6}Li$(n_{th},t)^4$He reactions obey the $1/v$ law in this neutron energy region.

Two kinds of measurements were performed using the accelerator d-d neutron source and the Am-Be isotopic neutron source, respectively. The experimental setups are schematically shown in Figs. 4(a) and 4(b), respectively. In the measurements, signals from the forward side and backward side of the GIC were measured independently; namely, the two PDA14 boards were set to the single board operation mode.

The accelerator-based measurement was performed at the 4.5 MV Van de Graaff accelerator of Peking University. Fast neutrons were produced through the D$(d,n)^3$He reaction using a deuterium gas target. The neutron energy was 4.0 MeV with the energy spread of 0.23 MeV. The fast neutron flux was monitored and normalized by a small ^{238}U fission chamber as shown in Fig. 4(a). The GIC detector was enclosed by paraffin blocks with a thickness of 20 cm to moderate the neutrons. Monte Carlo simulation showed that inside the paraffin moderator about 95% of neutrons were low-energy

TABLE I. Duration of the measurements for the Am-Be source-based measurement (in hours).

	^{10}B sample		^{6}LiF sample		Total
	Foreground	Background	Foreground	Background	
First run	13.3	41.4	16.2	17.9	88.8
Second run	22.0	20.3	30.0	26.8	99.1
Third run	36.0	35.6	50.3	48.9	170.8

neutrons with the energy below 0.01 MeV. Details of the accelerator-based measurement can be found in Ref. [5].

The accelerator-based measurement was performed once in July 2016, which included two runs. In the first run, side B of the ^{10}B sample and the ^{6}LiF sample was set at the backward direction of the GIC (facing the deuterium gas target). In the second run, the GIC was turned 180° along its axis and the measurement was repeated. The deuteron beam current was about 1.5 μA during the measurement. The duration of measurement per run for each sample was about 40 min and the total beam time was about 3 h.

In the Am-Be source-based measurement, the neutron source intensity was about $1.06 \times 10^6\ n/\mathrm{s}$ [7]. The Am-Be source was placed inside the paraffin blocks to moderate the neutrons as shown in Fig. 4(b). Since the counting rates of the $^{10}\mathrm{B}(n_{th},\alpha)^7\mathrm{Li}$ and $^{6}\mathrm{Li}(n_{th},t)^4\mathrm{He}$ reactions were rather low in this case (about 171 and 100 counts per hour, respectively), long measurement durations were needed and it was necessary to measure the background without the neutron source.

In order to study whether the number of ^{10}B atoms decreases over a period of time, the Am-Be source-based measurement was performed three times, in September, October, and December 2016, respectively. The durations of the foreground and background measurements for the $^{10}\mathrm{B}(n_{th},\alpha)^7\mathrm{Li}$ and $^{6}\mathrm{Li}(n_{th},t)^4\mathrm{He}$ reactions are listed in Table I. The durations of measurements were used to normalize the neutron fluence.

A characteristic two-dimensional pulse-amplitude spectrum of the grid versus the anode for the $^{6}\mathrm{Li}(n_{th},t)^4\mathrm{He}$ and $^{10}\mathrm{B}(n_{th},\alpha)^7\mathrm{Li}$ reactions is shown in Figs. 5(a) and 5(b), respectively. Signal islands of identified particle groups are clearly visible as shown in the figures.

The data processing method is similar to that in Ref. [5]. The anode spectra of the particles from the $^{6}\mathrm{Li}(n_{th},t)^4\mathrm{He}$ and $^{10}\mathrm{B}(n_{th},\alpha)^7\mathrm{Li}$ reactions were obtained after the projection to the anode. The spectra are shown in Figs. 6(a) and 6(b), respectively. In addition, the anode spectra were simulated by taking into account the energy loss of the products in the sample and the wall effect of the sample position [8]. In general, the simulated spectra agree well with the measured ones. Due to the high detection threshold, not all the lithium particles (Li_0 and Li_1) from the $^{10}\mathrm{B}(n_{th},\alpha)^7\mathrm{Li}$ reaction were detected, as shown in Fig. 6(b).

The triton and $\alpha_0 + \alpha_1$ peaks were used to obtain the event counts of the $^{6}\mathrm{Li}(n_{th},t)^4\mathrm{He}$ and $^{10}\mathrm{B}(n_{th},\alpha)^7\mathrm{Li}$ reactions, respectively. The detection efficiency of the triton and $\alpha_0 + \alpha_1$ particles were calculated using the simulated spectra.

After normalization of the neutron fluence, the number of ^{10}B atoms was calculated by Eq. (1). The results are listed in Table II. In the table, side A indicates the number of ^{10}B atoms in the position of holes and side B the total number of ^{10}B atoms; A/B indicates the ratio of side A to side B. In general, good agreements were obtained between the results of the four measurements using the accelerator and the Am-Be neutron sources. In addition, the ratio of A/B agreed well with that calculated by the geometry of the Ta frame (44.60%).

As can be seen from Table II, the number of ^{10}B atoms in the sample did not decrease over a period of about half a year. The measurement of the $^{10}\mathrm{B}(n,t2\alpha)$ three-body reaction was performed in November 2016, which was between the second and third Am-Be source-based measurements.

The average value of the accelerator measurement results (0.55×10^{19}) was taken as the number of ^{10}B atoms in the position of the holes with the uncertainty of 3.5%. The major source of uncertainty was the uncertainty of the number of ^{6}Li atoms, which was 3%. The thickness of the ^{10}B deposit was about 18.1 $\mu\mathrm{g/cm}^2$ calculated using the measured number of ^{10}B atoms.

IV. MEASUREMENT OF THE $^{10}\mathrm{B}(n,t2\alpha)$ REACTION

The measurement of the $^{10}\mathrm{B}(n,t2\alpha)$ three-body reaction was performed at the 4.5 MV Van de Graaff accelerator

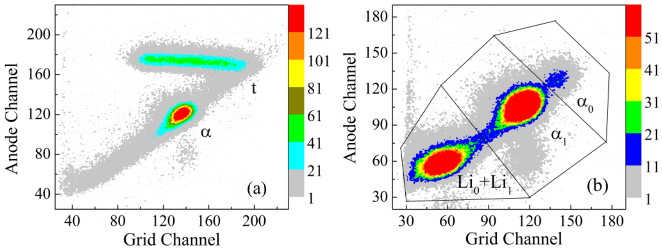

FIG. 5. Grid-anode two-dimensional spectrum obtained in the accelerator-based measurement (a) for the $^{6}\mathrm{Li}(n_{th},t)^4\mathrm{He}$ reaction and (b) for the $^{10}\mathrm{B}(n_{th},\alpha)^7\mathrm{Li}$ reaction.

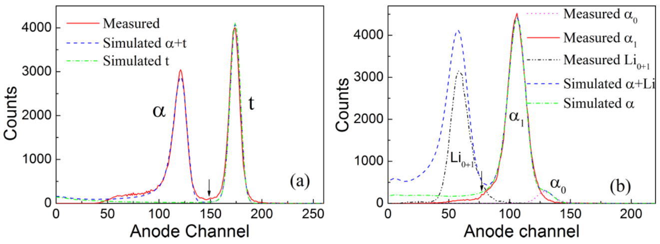

FIG. 6. Anode spectrum obtained in the accelerator-based measurement (a) for the $^{6}\mathrm{Li}(n_{th},t)^4\mathrm{He}$ reaction and (b) for the $^{10}\mathrm{B}(n_{th},\alpha)^7\mathrm{Li}$ reaction.

TABLE II. Measured results of the number of ^{10}B atoms and the uncertainties.

	Side A ($\times 10^{19}$)	Side B ($\times 10^{19}$)	A/B
Accelerator, first run	0.564 (3.5%)	1.234 (3.5%)	45.7%
Accelerator, second run	0.535 (3.5%)	1.150 (3.5%)	46.5%
Accelerator average[a]	0.55 (3.5%)	1.19 (3.5%)	46.2%
Am-Be, first run		1.26 (5.3%)[b]	
Am-Be, second run	0.54 (4.7%)	1.16 (4.3%)	46.5%
Am-Be, third run	0.53 (4.2%)	1.20 (3.9%)	44.2%

[a] Average value of the results of the first and second runs.

[b] Only the signals of side B were measured.

of Peking University at $E_n = 4.0$, 4.5, and 5.0 MeV. The experimental setup included three main parts: the neutron source, the GIC, and a BF$_3$ long counter. Details of the setup can be found in Ref. [2]. The BF$_3$ counter was used as the neutron flux monitor. The normal line of the electrodes of the GIC and the axis of the BF$_3$ counter were along the deuteron beam line.

Fast neutrons were produced by the D(d,n)^{3}He reaction using a deuterium gas target. For neutrons with energy of 4.0, 4.5, and 5.0 MeV, the energies were 0.21, 0.19, and 0.16 MeV, respectively [9]. The deuteron beam current was about 2.5 $\sim$ 3.5 μA.

The GIC was used as the charged particle detector. The working gas of the chamber was a mixture of krypton with 2.7% carbon dioxide. The pressures of the working gas and the high voltages applied on the cathode and anode are listed in Table III. Each grid electrode was grounded through a 20 MΩ resistor. The gas pressures were chosen to guarantee that the length of the triton ionization track along the 0° direction was less than about 80% of the distance between the grid and the cathode, so that the amplitudes of the grid signals of all of the three-particle events were high enough to be detected.

The measurement was first performed at $E_n = 4.0$ MeV, and then at 5.0 MeV, and finally at 4.5 MeV. At each neutron energy point, the experimental process in turn was as follows: (1) compound α-source measurement for energy calibration of the DAQ system and for determination of the electron drift time of events starting from the cathode, (2) foreground measurement with the ^{10}B sample, (3) background measurement with the background sample, (4) ^{238}U fission fragments measurement for determination of the absolute neutron flux, and (5) compound α-source measurement again to check the stability of the DAQ system. The beam durations for the foreground, background, and fission fragment measurements at $E_n = 4.0$, 4.5, and 5.0 MeV are shown in Table IV. The total beam duration was about 68 h. The neutron intensity was monitored by the BF$_3$ long counter with LABVIEW data acquisition software [2]. When the accelerator was in steady operation, the fluctuations of the neutron intensity were within 10%.

TABLE III. Gas pressures and cathode and anode high voltages of the GIC in the measurement.

E_n (MeV)	4.0	4.5	5.0
Pressure (atm)	1.8	2.0	2.3
HV (V)	−2500/1360	−2780/1400	−3280/1720

TABLE IV. Beam durations (in hours) for the foreground, background, and fission fragment measurements at $E_n = 4.0$, 4.5, and 5.0 MeV.

E_n (MeV)	4.0	4.5	5.0
Foreground	12.3	11.3	11.2
Background	9.3	8.2	8.2
Fission	2.6	2.3	2.4
Total	24.2	21.8	21.8

In the data processing for the α source, two kinds of two-dimensional (2D) spectra were obtained. The first kind was the pulse-height spectrum of the grid versus the anode, and the second one was the drift time versus the anode pulse height as shown in Figs. 7(a) and 7(b), respectively. The energies of the four α-particle groups, namely α_1, α_2, α_3, and α_4, are 4.775, 5.155, 5.499, and 5.805 MeV, which are emitted from the ^{234}U, ^{239}Pu, ^{238}Pu, and ^{244}Cm isotopes, respectively. Using the pulse-height 2D spectrum in Fig. 7(a), the energy-channel relations for the anode and the grid were calibrated.

The drift time is defined as the period from the start moment of the ionization track movement to the end moment when all the electrons are collected by the anode. For the ionization track starting from the cathode, the drift time is fixed; for the one born in the working gas of the GIC and that does not hit the cathode, the drift time is distributed over a wide time range [10]. Using the 2D spectrum in Fig. 7(b), a time window was determined for the drift time of the ionization track starting from the cathode. The time window was from 108 to 128 channels, which was about 3.2–3.8 μs. This time window will be used to reject background events in the data processing for the ^{10}B(n,$t2\alpha$) reaction.

For the experimental data processing of the ^{10}B reactions induced by the fast neutrons, the pulse-height two-dimensional spectrum of the grid versus the anode was first obtained. Figures 8(a) and 8(b) show the forward and backward 2D spectra after background subtraction, respectively. On the basis of the predicted 2D spectra as shown in Fig. 9 in the first paper [1], the events' positions for the ^{10}B(n,$t2\alpha$) plus the ^{10}B(n,α)^{7}Li reactions in the forward and backward 2D spectra

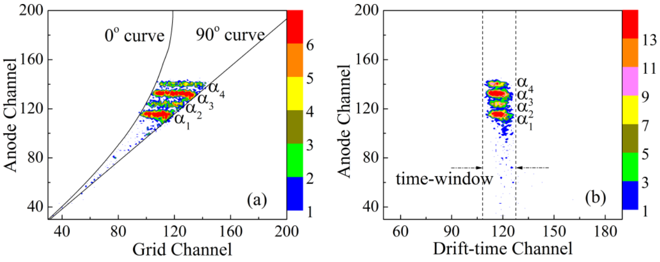

FIG. 7. Two-dimensional spectrum of the α source at $E_n = 4.0$ MeV: (a) the grid pulse height versus the anode pulse-height and (b) the drift time versus the anode pulse height.

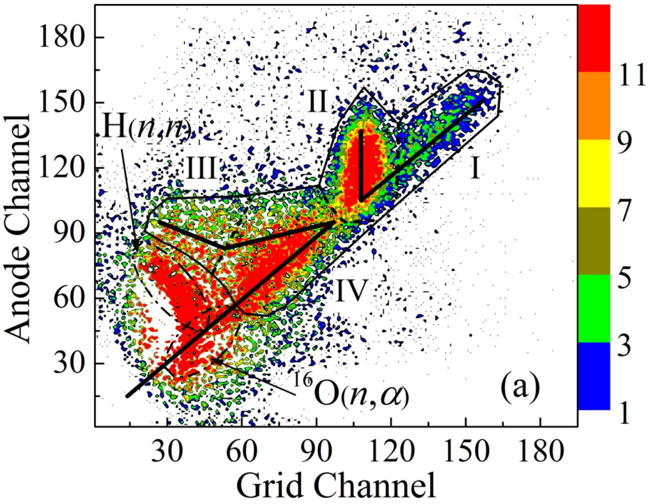

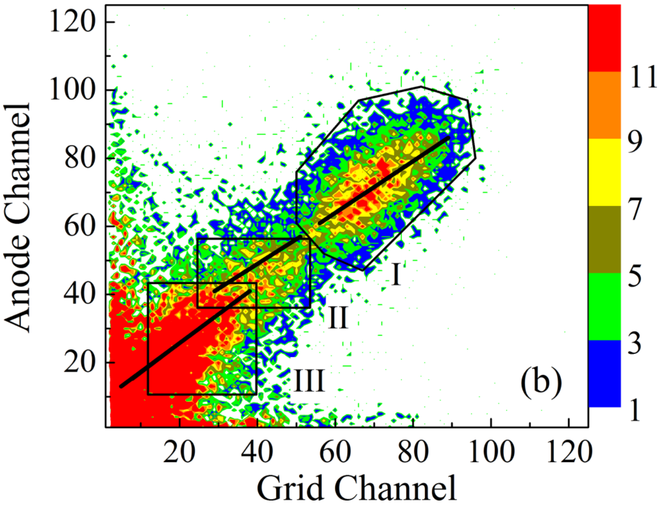

FIG. 8. Grid-anode two-dimensional spectrum of the ^{10}B reaction induced by neutrons with $E_n = 4.0\,\text{MeV}$, (a) forward and (b) backward.

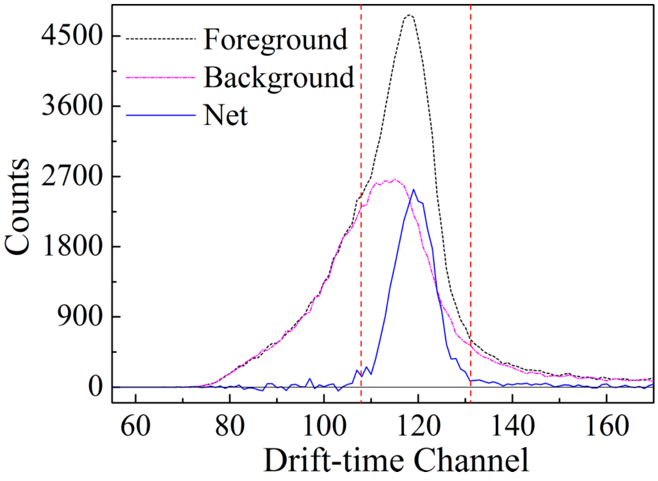

FIG. 9. Drift-time spectrum for the foreground and background events in the effective event area at $E_n = 4.0\,\text{MeV}$.

are marked as the five thick solid lines shown in Fig. 8(a) and the three thick solid lines shown in Fig. 8(b), respectively.

In the forward spectrum, the effective event area for the ^{10}B(n,$t2\alpha$) and ^{10}B(n,α)^{7}Li reactions was determined as shown by the closed solid curve in Fig. 8(a). Using the effective event area, interferences from the H(n,n)p and ^{16}O(n,α)^{13}C reactions are rejected. The effective event area could be further divided into four parts: Part I corresponds to the leaking events from the (n,α) reaction, part II is the forward α events from the (n,α) reaction, part III is the forward triton events from the ^{8}Be channel of the (n,$t2\alpha$) reaction, and part IV contains both the forward α and triton events from the ^{8}Be, ^{7}Li**, and breakup channels of the (n,$t2\alpha$) reaction and the forward ^{7}Li events from the (n,α) reaction. As can be seen from the figure, the leaking events and the forward α events from the (n,α) reaction separate well from the (n,$t2\alpha$) reaction events, while the (n,$t2\alpha$) reaction events overlap with the forward ^{7}Li events from the (n,α) reaction.

For the backward spectrum as shown in Fig. 8(b), part I corresponds to backward α events from the (n,α) reaction, part II is the backward triton events from the ^{8}Be channel of the (n,$t2\alpha$) reaction, and part III contains both the backward α and triton events from the ^{8}Be, ^{7}Li**, and breakup channels of the (n,$t2\alpha$) reaction and the ^{7}Li events from the (n,α) reaction. Likewise, in the backward spectrum the backward α events from the (n,α) reaction separate well from the (n,$t2\alpha$) reaction events, while the (n,$t2\alpha$) reaction events overlap with the backward ^{7}Li events from the (n,α) reaction.

In addition to the pulse-height information (i.e., the effective event area in the forward spectrum), the drift-time information can be employed to further reduce the background. For the events in the effective event area, the corresponding pulse signals were processed again to get the drift-time distribution. The results are shown in Fig. 9. It can be found that the drift-time distribution of the net events lay well inside the time window determined by the data of the α-source measurement. Nearly half of the background events can be rejected through the selection of the time window.

The events of the ^{10}B(n,$t2\alpha$) reaction overlap with those of the ^{10}B(n,α)^{7}Li reaction in the forward and backward spectra. The forward plus backward total-energy spectrum can be used to separate the two reactions and obtain their event counts. After event selection by the effective event area and the time window, the total-energy spectrum was obtained by adding up the normalized pulse height of the forward and backward signals for the effective events. The results are shown in Fig. 10. The event peaks of the ^{10}B(n,$t2\alpha$) and ^{10}B(n,α)^{7}Li reactions can be seen clearly, although there is some degree of overlap between them. The calculated spectra (theoretically predicted in the previous paper) are also plotted in the figure. The spectrum of the "Calc. total" is the summation of "Calc. (n,α)" and "Calc. (n,$t2\alpha$)". As can be seen from the figure, the calculated spectrum agrees well with the measured one.

The first and straightforward way to obtain the event counts of the ^{10}B(n,$t2\alpha$) and ^{10}B(n,α)^{7}Li reactions from the total-energy spectrum is by spectrum unfolding. Using the calculated spectra of the (n,$t2\alpha$) and (n,α) reactions as shown in Fig. 10, the ratio of the event counts between the (n,$t2\alpha$)

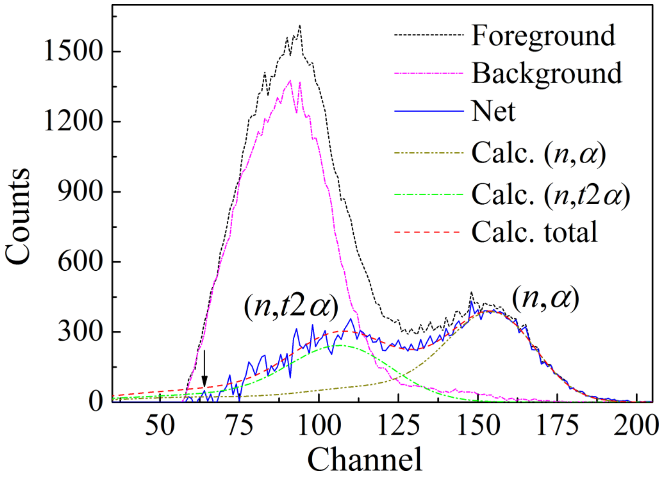

FIG. 10. The total-energy spectrum of the events selected by the effective event area and the time window at $E_n = 4.0$ MeV.

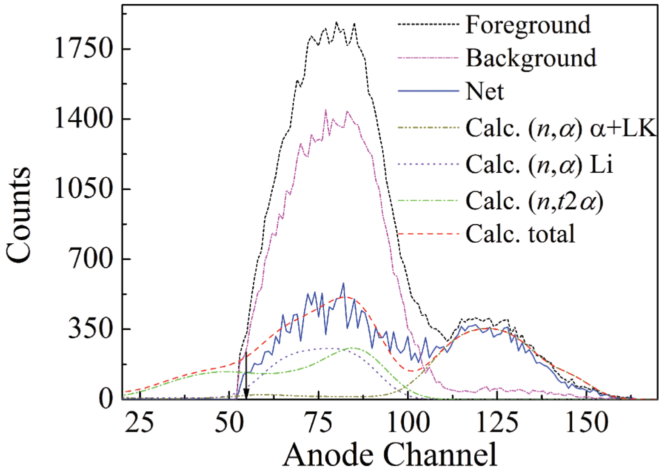

FIG. 12. Anode spectrum of the effective event area in the forward two-dimensional spectrum [as shown Fig. 8(a)] at $E_n = 4.0$ MeV.

and (n,α) reactions can be calculated; then the event counts of the two reactions can be obtained.

There is an another way to obtain the event counts of the $^{10}\mathrm{B}(n,t2\alpha)$ and $^{10}\mathrm{B}(n,\alpha)^7\mathrm{Li}$ reactions which is called the residual method. For the $^{10}\mathrm{B}(n,\alpha)^7\mathrm{Li}$ reaction, the forward α-particle + leaking events and the backward α-particle events are clearly visible in Figs. 8(a) and 8(b), respectively. The anode spectra of the forward α-particle + leaking events and the backward α-particle events were obtained after projection of areas I + II in Fig. 8(a) and area I in Fig. 8(b) to the anode. The anode spectra are shown in Figs. 11(a) and 11(b), respectively. The calculated spectra are also plotted in the figure. The detection efficiency of the forward α-particle + leaking events and the backward α-particle events were calculated using the calculated spectra. The event counts of the forward α-particle + leaking and the backward α-particle events were obtained from the anode spectra, and then the event counts of the (n,α) reaction were obtained by the summation of them. Since the total event counts of the $(n,t2\alpha)$ and (n,α) reactions were obtained from the total-energy spectrum, the event counts of the $(n,t2\alpha)$ reaction were obtained by subtracting the event counts of the (n,α) reaction from the total event counts. The event counts of the (n,α) reaction can be obtained accurately because of the clear structure in the 2D spectra; thus the event counts of the $(n,t2\alpha)$ reaction are more accurate from the residual method than those obtained by the spectrum unfolding method.

For the selection of time window, the detection efficiency was calculated using the drift-time spectrum as shown in Fig. 8. For the selection of effective event area, the detection efficiency was calculated using the calculated spectrum. Figure 12 shows the anode spectrum of the effective event area in the forward 2D spectrum. The calculated spectra of the $^{10}\mathrm{B}(n,t2\alpha)$ and $^{10}\mathrm{B}(n,\alpha)^7\mathrm{Li}$ reactions are plotted in the figure. The curve of "Calc. $(n,\alpha)\,\alpha$ + LK" is the spectrum of the forward α-particle + leaking events from the $^{10}\mathrm{B}(n,\alpha)^7\mathrm{Li}$ reaction and the curve

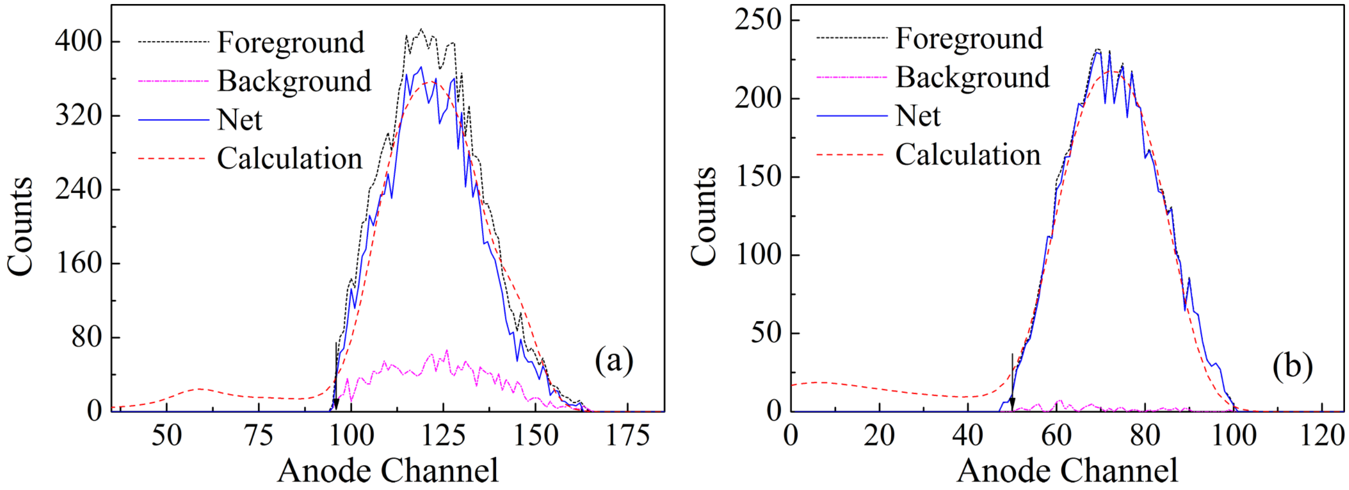

FIG. 11. Anode spectrum for the $^{10}\mathrm{B}(n,\alpha)^7\mathrm{Li}$ reaction at $E_n = 4.0$ MeV: (a) forward α-particle + leaking events and (b) backward α-particle events.

TABLE V. Results of cross sections for the ^{10}B$(n,t2\alpha)$ and ^{10}B$(n,\alpha)^7$Li reactions from the spectrum unfolding method and the residual method.

E_n (MeV)	$\sigma_{(n,t2\alpha)}$ (mb)			$\sigma_{(n,\alpha)}$ (mb)		
	Unfolding	Residual	Difference[a]	Unfolding	Residual	Difference[a]
4.0	182	155	17.0%	257	277	7.2%
4.5	216	194	11.3%	193	211	8.5%
5.0	164	185	11.3%	162	144	12.5%

[a] The ratio of the difference of "unfolding" and "residual" to the "residual."

of "Calc. (n,α) Li" is that of the forward ^{7}Li events. The detection efficiencies of the forward α-particle + leaking events and forward ^{7}Li events from the (n,α) reaction and the $(n,t2\alpha)$ reaction events can be obtained by the calculated spectra with the threshold shown as the arrow in Fig. 12. The correction factors were about 75% for the ^{10}B$(n,t2\alpha)$ reaction and about 96% for the ^{10}B$(n,\alpha)^7$Li reaction.

The spectrum of the fission fragments from the ^{238}U(n,f) reaction was used to obtain the fission counts, and the fission counts were used to determine the absolute neutron flux. Details of the data processing method for the fission spectrum can be found in Ref. [2]. Taking the cross section of the ^{238}U(n,f) reaction as the reference, the cross section of the ^{10}B$(n,t2\alpha)$ and ^{10}B$(n,\alpha)^7$Li reactions σ can be calculated by the following equation:

$$\sigma = \sigma_f \frac{N_{\mathrm{U8}}}{N_{\mathrm{B10}}} \frac{N'_\alpha N_{\mathrm{BF3}-f}}{N'_f N_{\mathrm{BF3}-\alpha}}, \quad (2)$$

where σ_f is the cross section of the ^{238}U(n,f) reaction taken from the standard library [6]; N_{U8} and N_{B10} are the number of ^{238}U and ^{10}B atoms in the samples, respectively; N'_α and N'_f are the event counts of the ^{10}B$(n,t2\alpha)$ [or ^{10}B$(n,\alpha)^7$Li] and ^{238}U(n,f) reactions, respectively; and $N_{\mathrm{BF3}-\alpha}$ and $N_{\mathrm{BF3}-f}$ are the counts of the neutron flux monitor (BF$_3$ long counter) in the measurements of ^{10}B and ^{238}U samples, respectively.

Cross sections of the ^{10}B$(n,t2\alpha)$ and ^{10}B$(n,\alpha)^7$Li reactions were calculated using the event counts from the spectrum unfolding method and the residual method. The results are listed in Table V. As can be seen from the table, results of the two methods generally agree with each other. For the ^{10}B$(n,t2\alpha)$ reaction, the difference of the two methods' result is relatively large at $E_n = 4.0$ MeV due to the lower value of the cross section. The difference of the ^{10}B$(n,\alpha)^7$Li reaction is small due to the large Q value and the lower influence from the background.

Since the event counts obtained by the residual method are more accurate, cross sections from the residual method are taken as the final results. For the ^{10}B$(n,\alpha)^7$Li reaction, in addition to the total cross section, cross sections of the leaking, forward α, and backward α (in the laboratory reference system) are also measured. The final cross sections and the uncertainties for the ^{10}B$(n,t2\alpha)$ and ^{10}B$(n,\alpha)^7$Li reactions are shown in Table VI.

According to the law of error propagation, the relative uncertainties of the cross section measured through Eq. (2) can be calculated using the following equation:

$$\frac{\Delta\sigma}{\sigma} = \sqrt{\left(\frac{\Delta\sigma_f}{\sigma_f}\right)^2 + \left(\frac{\Delta N_{\mathrm{U8}}}{N_{\mathrm{U8}}}\right)^2 + \left(\frac{\Delta N_{\mathrm{B10}}}{N_{\mathrm{B10}}}\right)^2 + \left(\frac{\Delta N'_\alpha}{N'_\alpha}\right)^2 + \left(\frac{\Delta N'_f}{N'_f}\right)^2 + \left(\frac{\Delta N_{\mathrm{BF3}-\alpha}}{N_{\mathrm{BF3}-\alpha}}\right)^2 + \left(\frac{\Delta N_{\mathrm{BF3}-f}}{N_{\mathrm{BF3}-f}}\right)^2}, \quad (3)$$

where the uncertainty of fission cross section σ_f is 0.8%; the uncertainties of the numbers of ^{238}U and ^{10}B atoms are 1.3% [2] and 3.5%, respectively; and the uncertainty of the fission counts N'_f is 3.1% [2]. The number of $N_{\mathrm{BF3}-\alpha}$ and $N_{\mathrm{BF3}-f}$ are about $10^7 \sim 10^8$, so their uncertainty can be neglected. The major source of uncertainty is the uncertainty of the event counts N'_α. The uncertainty of the event counts for the ^{10}B$(n,t2\alpha)$ and ^{10}B$(n,\alpha)^7$Li reactions was calculated using again the law of error propagation. Taking the ^{10}B$(n,t2\alpha)$ reaction as the example, in the residual method the event count C_{3B} was calculated by the following equation:

$$C_{\mathrm{3B}} = \frac{(C_{f-coi} - k_{fb}C_{b-coi})/\varepsilon_{\mathrm{DT}} - C_{\mathrm{2B}}\varepsilon_{\mathrm{2B}}}{\varepsilon_{\mathrm{3B}}}, \quad (4)$$

where C_{f-coi} and C_{b-coi} are the counts of the foreground and background total-energy spectrum, respectively; k_{fb} is the normalization factor for the subtraction of background from the foreground spectrum (using the counts of the BF$_3$ counter); C_{2B} are the event counts of the ^{10}B$(n,\alpha)^7$Li reaction obtained by the residual method; $\varepsilon_{\mathrm{DT}}$ is the correction factor for the selection of the drift-time window; and $\varepsilon_{\mathrm{3B}}$ and $\varepsilon_{\mathrm{2B}}$ are the correction factors for the selection of the effective event area for the ^{10}B$(n,t2\alpha)$ and ^{10}B$(n,\alpha)^7$Li reactions, respectively. According to the law of error propagation, the uncertainties of C_{3B} can be calculated by the following equation:

$$(\Delta C_{\mathrm{3B}})^2 = \frac{C_{f-coi} + (C_{b-coi}\Delta k_{fb})^2 + (k_{fb})^2 C_{b-coi}}{(\varepsilon_{\mathrm{3B}}\varepsilon_{\mathrm{DT}})^2} + \frac{(\varepsilon_{\mathrm{2B}}\Delta C_{\mathrm{2B}})^2 + (C_{\mathrm{2B}}\Delta\varepsilon_{\mathrm{2B}})^2}{(\varepsilon_{\mathrm{3B}})^2} + \left(C_{\mathrm{3B}}\frac{\Delta\varepsilon_{\mathrm{3B}}}{\varepsilon_{\mathrm{3B}}}\right)^2. \quad (5)$$

TABLE VI. Measured results of cross sections for the ^{10}B(n,$t2\alpha$) and ^{10}B(n,α)^{7}Li reactions.

E_n (MeV)	$\sigma_{(n,t2\alpha)}$ (mb)	$\sigma_{(n,\alpha)}$ (mb)			
		Total	Leaking	Forward α	Backward α
4.0	155 (19%)	277 (7%)	35 (9%)	143 (11%)	99 (9%)
4.5	194 (15%)	211 (7%)	30 (10%)	107 (11%)	74 (9%)
5.0	185 (23%)	144 (7%)	22 (10%)	72 (12%)	50 (9%)

The uncertainties of C_{f-coi} and C_{b-coi} are the statistical error, and the formulas $\Delta C_{f-coi} = \sqrt{C_{f-coi}}$ and $\Delta C_{b-coi} = \sqrt{C_{b-coi}}$ were used in the derivation of Eq. (5). The relative uncertainties of $\varepsilon_{3\mathrm{B}}$ and $\varepsilon_{2\mathrm{B}}$ are 10% and 1%, respectively. The major source of uncertainty for $C_{3\mathrm{B}}$ is the uncertainty of the normalization factor k_{fb}. The uncertainty of k_{fb} is 1% at $E_n = 4.0$ and 4.5 MeV and 3% at 5.0 MeV.

The present results of the ^{10}B(n,$t2\alpha$) and ^{10}B(n,α)^{7}Li reactions are compared with those of the existing measurements and evaluations as shown in Fig. 13. For the ^{10}B(n,$t2\alpha$) reaction, as shown in Fig. 13(a), the measurement method used by Frye *et al.* [11] was the boron-loaded emulsion; Wyman *et al.* [12], Qaim and Wolfle [13], and Suhaimi *et al.* [14] used the tritium counting; and Davis *et al.* [15] and Ivanova *et al.* [16] used the gridded ionization chamber with ^{10}B gas sample. As mentioned in the first paper [1], cross sections measured by the boron-loaded emulsion and tritium counting method are generally higher than those measured by the method of the GIC gas sample. The present results, measured by the method of the GIC thin-film sample, agree with those measured by the boron-loaded emulsion and tritium counting method. In the present measurement, the wall effect of the GIC can be avoided completely by choosing the pressure of the working gas properly as shown in Table III. In addition, the effective event area in the forward 2D spectrum and the time window in the drift-time spectrum are used to reject the background. We speculate that the wall effect and the background subtraction are the reasons that the results measured by the GIC gas sample are low.

Generally, the present results of the ^{10}B(n,$t2\alpha$) reaction agree with the evaluated results of the ENDF/B-VII.1, JENDL-4.0, and CN-RAC2016 libraries [17]. The trend of our results agree better with that of the CN-RAC2016 library, especially at $E_n = 4.5$ and 5.0 MeV. The errors of the present cross sections are relatively large, as shown in Table VI, and result mainly from the error of the normalization factor of the neutron flux between foreground and background spectra. Instead of the BF$_3$ counter, the ^{238}U sample is planned to be used to monitor the neutron flux to make the normalization factor more accurate. In addition, further measurements are needed at more neutron energy points to determine the trend of the excitation curve of the ^{10}B(n,$t2\alpha$) reaction.

In principle, the contributions of the ^{7}Li**, ^{8}Be, and breakup channels in the ^{10}B(n,$t2\alpha$) reaction can be obtained using the forward spectrum (as shown in Fig. 12) because the forward spectra of the three channels are different. However, in the present measurement, the energy resolution was modest and the structure of the forward spectrum was not clear enough to obtain any proper information of the proportions of the three channels. However, in the backward grid-anode 2D spectrum as shown in Fig. 9(b) in the first paper [1], the triton events of the ^{8}Be channel separate from other three-body and two-body events to some degree. From the measured backward grid-anode 2D spectra, it is found that the contribution of the ^{8}Be channel in the backward spectrum becomes less from 4.0 to 5.0 MeV; at $E_n = 4.0$ MeV, the contribution is more than 20% and at $E_n = 5.0$ MeV less than 10%. Further experiments are needed to confirm the above qualitative conclusion and

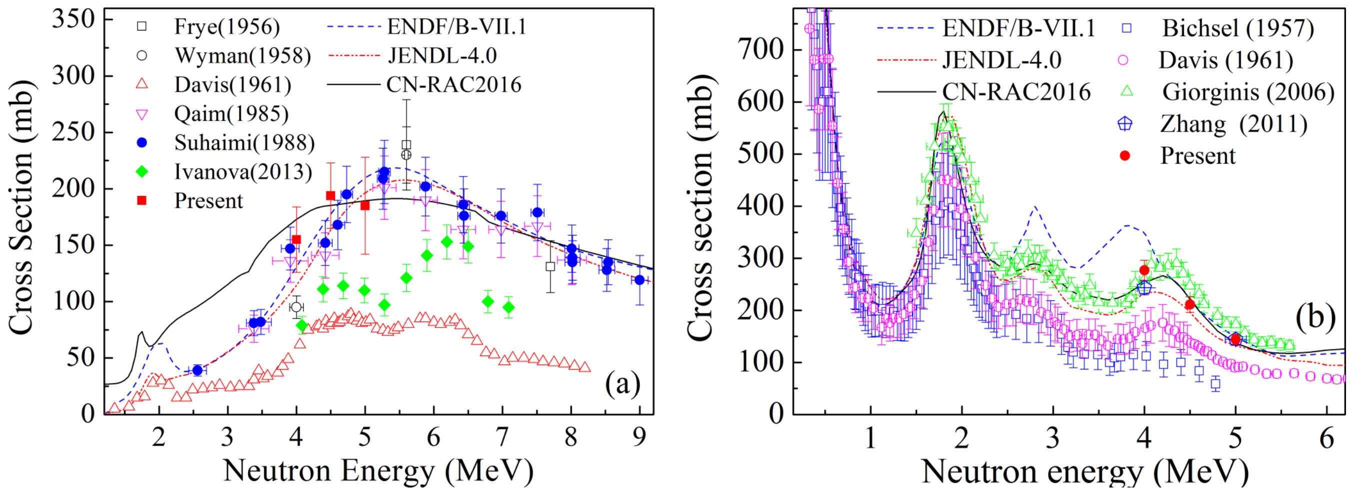

FIG. 13. Present cross sections compared with the existing measurements and evaluations (a) for the ^{10}B(n,$t2\alpha$) reaction and (b) for the ^{10}B(n,α)^{7}Li reaction.

study the intermediate mechanism of the three-body reaction quantitatively by improving the energy resolution of the GIC spectrometer.

Figure 13(b) shows the cross sections of the ^{10}B$(n,\alpha)^7$Li reaction. All the measurements were performed using the GIC detector, where Bichsel and Bonner [18] and Davis *et al.* [15] used the ^{10}B gas sample and Giorginis and Khryachkov [19] and Zhang *et al.* [20] used the ^{10}B solid sample. The present results agree well with those of Giorginis and Khryachkov and Zhang *et al.* In addition, the present results, as well as Giorginis and Khrychkov's and Zhang *et al.*'s results, support the data of the CN-RAC2016 library. More measurements are needed to classify the discrepancies among the libraries in the neutron energies below 4.0 MeV.

For the ^{10}B$(n,\alpha)^7$Li reaction at $E_n = 4.0, 4.5$, and 5.0 MeV, the ratios of the leaking cross section to the total cross section are 13%, 14%, and 15%, respectively; the ratios of the forward α cross section to the backward α cross section (in the laboratory reference system) are 1.44, 1.45, and 1.44 at $E_n = 4.0$, 4.5, and 5.0 MeV, respectively. The two ratios remain a constant within the uncertainties from 4.0 to 5.0 MeV. For the results of Zhang *et al.* [20], the ratios of the leaking cross section to the total cross section are 16% and 15% at $E_n = 4.0$ and 5.0 MeV; the ratios of the forward α cross section to the backward α cross section are 1.23 and 1.56, respectively. Differences exist between the present and Zhang *et al.*'s results of the ratios of the forward α cross section to the backward α cross section and more measurements are needed to classify the deviations.

V. CONCLUSIONS

A new digital DAQ system for the GIC detector was developed based on the high-speed WFD. A versatile data-acquisition software was developed using the LABVIEW language to control the digitizers (PDA14) and perform online data processing. In order to improve the antinoise performance of the system, the digitizers work in the external trigger mode and the TCU was used to produce the external trigger signals for each digitizer. By the new WFD-based GIC spectrometer, double-coincidence measurements can be achieved which are the grid-anode and the forward-backward coincidences.

A thin-film ^{10}B sample was designed and prepared. The ^{10}B sample consists of four components: the ^{10}B deposit, the aluminum-film backing as the substrate of ^{10}B deposit, the tantalum frame bearing the aluminum backing, and the aluminum washer to fix and flatten the tantalum frame. The number of ^{10}B atoms was determined by the relative comparison method using the thermal neutron induced ^{10}B$(n_{th},\alpha)^7$Li and ^{6}Li$(n_{th},t)^4$He reactions with a ^{6}LiF sample as the reference. Both the accelerator *d-d* neutron source and the Am-Be isotopic neutron source were used to produce neutrons. The number of ^{10}B atoms was measured four times over a period of about half a year. It was found that the number of ^{10}B atoms did not decrease over the period of half a year.

The ^{10}B$(n,t2\alpha)$ three-body reaction was measured at $E_n =$ 4.0, 4.5, and 5.0 MeV using the 4.5 MV Van de Graaff accelerator of Peking University. In the data processing, the effective event area in the forward two-dimensional spectrum and the time window in the drift-time spectrum were employed to reject the background events. Cross sections of both the ^{10}B$(n,t2\alpha)$ three-body and ^{10}B$(n,\alpha)^7$Li two-body reactions were obtained. The present results of the ^{10}B$(n,t2\alpha)$ reaction are higher than those measured by the method of the GIC gas sample and agree with those measured by the boron-loaded emulsion and tritium counting methods. In addition, the present results of the ^{10}B$(n,t2\alpha)$ reaction agree with the evaluated results of the ENDF/B-VII.1, JENDL-4.0, and CN-RAC2016 libraries. Our results of the ^{10}B$(n,\alpha)^7$Li reaction agree well with those of the recent measurements and the data of the CN-RAC2016 library.

Further experiments are needed to reduce the error of the present results through using the ^{238}U sample to monitor and normalize the neutron flux. Systematic measurements at more neutron energies are needed to study the trend of the excitation curves of the ^{10}B$(n,t2\alpha)$ and ^{10}B$(n,\alpha)^7$Li reactions, especially below 4.0 MeV. In addition, the intermediate mechanism of the three-body reaction will be studied by improving the energy resolution of the GIC spectrometer.

ACKNOWLEDGMENTS

The authors are grateful to the operation team of the 4.5 MV Van de Graff accelerator of Peking University. Prof. Zhenpeng Chen from Tsinghua University is acknowledged for providing the CN-RAC2016 evaluation library. Special thanks are given to Dr. Qiwen Fan from CIAE for the skillful preparation of the thin-film ^{10}B samples. The present work was financially supported by the National Natural Science Foundation of China (Grant No. 11475007), China Nuclear Data Center, and the Science and Technology on Nuclear Data Laboratory.

---

[1] Z. Wang, H. Bai, L. Zhang, H. Jiang, Y. Lu, J. Chen, G. Zhang, Y. M. Gledenov, M. V. Sedysheva, and G. Khuukhenkhuu, Phys. Rev. C **96**, 044620 (2017).

[2] Z. Wang, X. Fan, L. Zhang, H. Bai, J. Chen, G. Zhang, Y. M. Gledenov, M. V. Sedysheva, L. Krupa, and G. Khuukhenkhuu, Phys. Rev. C **92**, 044601 (2015).

[3] A. Al-Adili, F.-J. Hambsch, S. Oberstedt, S. Pomp, and S. Zeynalov, Nucl. Instrum. Methods A **624**, 684 (2010).

[4] Q. Fan and G. Xu, Nucl. Instrum. Methods A **590**, 96 (2008).

[5] G. Zhang, J. Liu, Z. Xue, H. Wu, Y. Liu, X. Yuan, and X. Liu, Appl. Radiat. Isot. **69**, 858 (2011).

[6] Neutron cross-section standards (2006) and references (2015), https://www-nds.iaea.org/standards/

[7] J. Chen, P. Zhu, Y. Li, Z. Liu, and G. Zhang, Nucl. Instrum. Methods A **583**, 407 (2007).

[8] H. Bai, Z. Wang, L. Zhang, H. Jiang, Y. Lu, J. Chen, and G. Zhang, Appl. Radiat. Isot. **125**, 34 (2017).

[9] G. Zhang, Y. M. Gledenov, G. Khuukhenkhuu, M. V. Sedysheva, P. J. Szalanski, P. E. Koehler, Y. N. Voronov, J. Liu, X. Liu, J. Han, and J. Chen, Phys. Rev. Lett. **107**, 252502 (2011).

[10] V. A. Khriachkov, V. V. Ketlerov, V. F. Mitrofanov, and N. N. Semenova, Nucl. Instrum. Methods A **444**, 614 (2000).

[11] G. M. Frye, Jr. and J. H. Gammel, Phys. Rev. **103**, 328 (1956).
[12] M. E. Wyman, E. M. Fryer, and M. M. Thorpe, Phys. Rev. **112**, 1264 (1958).
[13] S. M. Qaim and R. Wolfle, Nucl. Phys. A **295**, 150 (1978).
[14] A. Suhaimi, R. Wolfle, S. M. Qaim, and G. Stocklin, Radiochim. Acta **40**, 113 (1986).
[15] E. A. Davis, F. Gabbard, T. W. Bonner, and R. Bass, Nucl. Phys. **27**, 448 (1961).
[16] T. A. Ivanova, I. P. Bondarenko, B. D. Kuzminov, Y. A. Kurachenko, N. N. Semenova, A. I. Sergachev, and V. A. Khryachkov, Bull. Russ. Acad. Sci.: Phys. **77**, 455 (2013).
[17] Nuclear Data Services, International Atomic Energy Agency, http://www-nds.iaea.org/
[18] H. Bichsel and T. W. Bonner, Phys. Rev. **108**, 1025 (1957).
[19] G. Giorginis and V. Khryachkov, Nucl. Instrum. Methods A **562**, 737 (2006).
[20] G. Zhang, X. Liu, J. Liu, Z. Xue, H. Wu, and J. Chen, Chin. Phys. Lett. **28**, 082801 (2011).